Published in final edited form as:
Doc Ophthalmol. 2009 June ; 118(3): 239–246. doi:10.1007/s10633-008-9154-5.

Detailed analysis of retinal function and morphology in a patient with autosomal recessive bestrophinopathy (ARB)

Christina Gerth✉,
Department of Ophthalmology and Vision Sciences, The Hospital for Sick Children, University of Toronto, Toronto, Canada

Robert J. Zawadzki,
Department of Ophthalmology and Vision Sciences, The Hospital for Sick Children, University of Toronto, Toronto, Canada

John S. Werner, and
Department of Ophthalmology & Vision Science, Vision Science and Advanced Retinal Imaging Laboratory (VSRI), University of California, Davis, USA

Elise Héon
Department of Ophthalmology and Vision Sciences, The Hospital for Sick Children, University of Toronto, Toronto, Canada

Abstract

The objective of the paper is to study the retinal microstructure and function in a patient with autosomal recessive bestrophinopathy (ARB). Retinal function and morphology assessment in a patient diagnosed with a biallelic mutation in the *BEST1* gene (heterozygote mutations: Leu88del17 and A195V) included: full-field electroretinogram (ffERG) and multifocal electroretinogram (mfERG), electro-oculogram (EOG) testing, and imaging with a high-resolution Fourier-domain optical coherence tomography (Fd-OCT) system (UC Davis Medical Center; axial resolution: 4.5 μm, acquisition speed: 9 frames/s, 1,000 A-scans/frame) combined with a flexible scanning head (Bioptigen Inc.). The 11-year old asymptomatic boy showed a well-demarcated retinopathy with deposits. Functional assessment revealed normal visual acuity, reduced central mfERG responses, delayed rod and rod-cone b-wave ffERG responses, and reduced light rise in the EOG. Fd-OCT demonstrated RPE deposits, photoreceptor detachment, elongated and thickened photoreceptor outer segments, but preserved inner retinal layers. In conclusion, ARB associated retinal dystrophy shows functional and morphological changes that overlap with classic Best disease. For the first time, high-resolution imaging provided in vivo evidence of RPE and photoreceptor involvement in ARB.

Keywords

Autosomal recessive bestrophinopathy; ARB; Fourier-domain OCT; Multifocal ERG; Electro-oculogram

Introduction

Retinal dystrophy associated with biallelic mutations in the *BEST1* gene was recently described by Burgess et al. and is now referred to as autosomal recessive bestrophinopathy (ARB) [1]. Clinical features of autosomal dominant classic Best disease caused by *BEST1* mutations [2–

Department of Ophthalmology, University of Rostock, Doberaner Street 140, Rostock 18055, Germany. e-mail: E-mail: chgerth@web.de.

4] and those of ARB have in common deep retinal deposits and reduction of the electro-oculogram (EOG) light rise. In vivo retinal imaging using time-domain optical coherence tomography (OCT) identified in a patient with ARB retinal edema and subretinal fluid between retinal pigment epithelium (RPE) and neurosensory retina [1]. Previous retinal layer analyses were limited by the image resolution of the time-domain OCT instrumentation. Using a higher-resolution Fourier-domain OCT (Fd-OCT) instrument, we demonstrated for the first time significant photoreceptor changes in a case with biallelic *BEST1* mutation.

Methods

A healthy and asymptomatic boy was referred to the Ocular Genetics Clinic at The Hospital for Sick Children in Toronto, Canada, for evaluation of ‘retinal flecks’ seen at a routine eye examination at age 11. His maternal side was of English/Dutch/Newfoundland origin; his paternal origin is unknown. His past medical and family history was unrevealing. Written informed consent was obtained from his guardians. The project was approved by The Research Ethics Board at The Hospital for Sick Children and by the UC Davis Institutional Review Board, and conducted in accordance with the Tenets of Helsinki.

Vision function

Vision function assessment included best-corrected monocular distance visual acuity (VA) on a logMAR scale using the backlit Early Treatment Diabetic Retinopathy Study Chart, color vision testing (Hardy–Rand–Rittler pseudoisochromatic plates under standard illumination) and measurement of contrast sensitivity (CS; Pelli–Robson Contrast Sensitivity charts). Monocular static and kinetic visual fields were obtained with the Humphrey Visual Field Analyzer (HFA II; program 24–2; Carl Zeiss Meditec, Inc., Dublin, CA) and Goldmann perimeter (target size III4e, I4e), respectively.

Full-field electroretinogram (ffERG) was recorded according to the ISCEV standard [5]. In addition, a bright flash ERG (244 cd s/m^2) was performed under scotopic and photopic conditions. Isolated rod photoreceptor responses were calculated by digitally subtracting the photopic responses from the combined scotopic and photopic response as described by Hood and Birch [6]. The multifocal electroretinogram (mfERG) was recorded with a stimulus-refractor unit (VERIS, vers.5.1, EDI, San Mateo, CA) on 61 scaled hexagons with a maximum flash intensity of 200 cd m^{-2}/75 Hz. Results of ffERG and mfERG were compared with age-matched control data. EOG responses were registered according to the ISCEV standard [7] (recordings were done before the new ISCEV EOG standard from 2006). Autofluorescence imaging was not available. Molecular genetic analyses were provided as a clinical service by the Carver laboratory (Iowa City, IA, USA).

Fourier-domain optical coherence tomography

Retinal image acquisition was achieved using a custom built, high-speed, high-resolution Fd-OCT system [8] (axial resolution: 4.5 μm; acquisition speed: 9 frames/s, 1,000 A-scans/frame) constructed at UC Davis with the scanning head mounted on an articulating arm (Bioptigen Inc., Durham, NC, USA). Horizontal scans of 6 mm length or a volumetric scan series permitting image acquisition over an area of 6 × 6 mm and OCT fundus reconstruction were registered through the macular area. Raw image data were post-processed, and retinal layers were identified as previously described (Fig. 1) [9,10].

Results

Visual acuity was nearly normal and stable over the past 3 years of our assessment. CS was reduced in both eyes. Detailed results of vision function tests are listed in Table 1.

Fundus examination revealed multiple yellowish-white, round, partially confluent lesions at the posterior pole and around the optic nerve with a well-demarcated edge. The lesions were predominant around the vascular arcades and the fovea. The left eye showed two areas with subretinal fibrosis (Fig. 2).

Two heterozygous mutations (Leu88del17 and A195V) in the *BEST1* gene were identified.

Electrophysiological findings

Full-field ERG revealed delayed rod and rod-cone b-wave responses in both eyes. The rod b-wave responses did not return to baseline within the recording window used. All response amplitudes were within normal limits (Table 1). Isolated rod photoreceptor responses using the bright flash stimulus showed normal implicit time and amplitude. Of interest is the pronounced negativity prior to OP1 in both eyes (Fig. 3). The mfERG responses were reduced and delayed within the central 10° (Fig. 4). EOG revealed a markedly reduced Arden ratio in both eyes with a dark trough after 8 min (amplitude 1.92 μV) and light peak 6 min from the start of the light phase.

Retinal microstructure

Macular scans demonstrated round- or dome-shaped deposits within the RPE reaching into the subretinal space. Large deposits extended up to the OPL in the left eye as shown in Fig. 2b. The RPE itself was thinned throughout the macula. Photoreceptor layers were detached from the RPE as shown in Fig. 2. Photoreceptor outer segments were thicker and elongated compared with normal control data. Small filament-like bridges were visible between the photoreceptor outer segment layer and the RPE. Verhoeff's membrane, the interface between cone photoreceptors and the RPE, was not identifiable in multiple scans of both eyes (Fig. 2). Inner retinal layers were unaffected.

Comment

Retinal dystrophy associated with biallelic mutations in *BEST1* is associated with RPE deposits and marked photoreceptor abnormalities. Signs of photoreceptor detachment resembled descriptions of patients with classic Best disease. Retinal imaging using lower-resolution time-domain OCT in patients with Best disease, which does not allow differentiation of photoreceptor layers and RPE, revealed RPE and photoreceptor detachment in those patients [11], accumulation of material on the outer retina, in the subretinal space or between RPE and outer retinal layers associated with subretinal fluid [12].

No histopathological data are available due to the novel ARB phenotype description of *BEST1* mutations. Histopathological data from a 27-year-old patient with classic Best disease demonstrated edematous ganglion cell, inner and outer plexiform layers in the central retina, atrophic photoreceptor outer segments, and diffusely abnormal RPE cells loaded with lipofuscin granules [13]. RPE and outer retina abnormalities were more advanced in the macular area with normal-appearing RPE outside the macula in older patients with classic Best disease [14,15]. Bakall et al. identified an up to 4-fold increase in A2E deposits in RPE cells in a 81-year old patient with Best disease [16]. Analysis of the granules suggested that RPE cells are not able to fully break down phagocytised photoreceptor outer segments [16]. The identified bridges in the patient presented here might represent unshedded disks leading to elongated outer segments.

The protein product bestrophin-1, locates at the baso-lateral plasma membrane of the RPE [17], is thought to play a regulatory role in the Ca^{2+} activated Cl^{-} channel [18,19]. Lipofuscin cytotoxicity leads to RPE cell dysfunction with consecutive photoreceptor degeneration [16].

We showed abnormal photoreceptor structure but unchanged inner retinal layers associated with abnormal cone mediated mfERG responses in the central retina. Isolated rod photoreceptor responses indicated by the bright flash ffERG were normal. The ffERG shows a negative ‘response’ prior to OP1. OPs are generated postsynaptic to the photoreceptors, possibly by amacrine, bipolar and/or interplexiform cells [20]. It is proposed that the short-latency scotopic OPs are generated through the cone pathway and the long-latency scotopic OPs through the rod pathways [21]. Therefore, the negativity prior to OP1 might point to changes within the cone pathway.

The rod and rod-cone b-wave implicit times might reflect abnormalities distal to the photoreceptors. The tests we performed cannot rule out focal photoreceptor abnormalities. The bright flash rod response indicates normal global rod photoreceptor function. We are not able to test rod function focally in areas with visible fundus changes and identified abnormalities in Fd-OCT scans. Focal cone photoreceptor function is not isolated either. The mfERG responses are a product of photoreceptor and bipolar cells [22]. Morphological OCT results indicated changes within the outer retina layers including photoreceptors and the interface between cone photoreceptors and the RPE (Verhoeff's membrane) in the scanned macular area. It is quite surprising that the patient's vision is normal despite the photoreceptor detachment from the RPE. From the tests performed, we are not able to determine the functional consequences of the identified morphological changes.

Burgess et al. reported reduced rod and cone ERG responses in all seven patients and delayed scotopic or photopic ERG responses in two and three patients, respectively [1]. Macular function evaluated by pattern ERG was mildly reduced to non-detectable in five patients [1] indicating ganglion cell dysfunction possibly including distal retinal layers [23].

Confirmation of this newly described phenotype associated with biallelic mutations in *BEST1* and functional analysis of the mutations will provide longitudinal information about photoreceptor morphology and function. High-resolution macular imaging together with electrophysiological testing will be important for advancing our understanding of this disease process.

Acknowledgments

This study was supported by NIH/NEI grant 014743 (JSW), Research to Prevent Blindness Senior Scientist Award (JSW), the Mira Godard Fund (EH) and the Albrecht Fund (JSW) in collaboration with Bioptigen, Inc. We thank Yesmino Elia for study coordination, Carmelina Trimboli-Heidler for fundus photography, and Tom Wright and Carole Panton for help with data analysis.

References

1. Burgess R, Millar ID, Leroy BP, et al. Biallelic mutation of BEST1 causes a distinct retinopathy in humans. Am J Hum Genet 2008;82:19–31. [PubMed: 18179881]
2. Petrukhin K, Koisti MJ, Bakall B, et al. Identification of the gene responsible for Best macular dystrophy. Nat Genet 1998;19:241–247. [PubMed: 9662395]
3. Stohr H, Marquardt A, Rivera A, et al. A gene map of the Best's vitelliform macular dystrophy region in chromosome 11q12–q13.1. Genome Res 1998;8:48–56. [PubMed: 9445487]
4. Marquardt A, Stohr H, Passmore LA, et al. Mutations in a novel gene, VMD2, encoding a protein of unknown properties cause juvenile-onset vitelliform macular dystrophy (Best's disease). Hum Mol Genet 1998;7:1517–1525. [PubMed: 9700209]
5. Marmor MF, Holder GE, Seeliger MW, Yamamoto S. Standard for clinical electroretinography (2004 update). Doc Ophthalmol 2004;108:107–114. [PubMed: 15455793]
6. Hood DC, Birch DG. Assessing abnormal rod photoreceptor activity with the a-wave of the electroretinogram: applications and methods. Doc Ophthalmol 1996;92:253–267. [PubMed: 9476593]

7. Marmor MF, Zrenner E. Standard for clinical electro-oculography. International society for clinical electrophysiology of vision. Arch Ophthalmol 1993;111:601–604. [PubMed: 8489436]
8. Wojtkowski M, Leitgeb R, Kowalczyk A, et al. In vivo human retinal imaging by Fourier domain optical coherence tomography. J Biomed Opt 2002;7:457–463. [PubMed: 12175297]
9. Zawadzki RJ, Jones SM, Olivier SS, et al. Adaptive-optics optical coherence tomography for high-resolution and high-speed 3D retinal in-vivo imaging. Opt Express 2005;13:8532–8546. [PubMed: 19096728]
10. Zawadzki RJ, Fuller AR, Wiley DF, et al. Adaptation of a support vector machine algorithm for segmentation and visualization of retinal structures in volumetric optical coherence tomography data sets. J Biomed Opt 2007;12:041206. [PubMed: 17867795]
11. Wabbels B, Preising MN, Kretschmann U, et al. Genotype-phenotype correlation and longitudinal course in ten families with Best vitelliform macular dystrophy. Graefes Arch Clin Exp Ophthalmol 2006;244:1453–1466. [PubMed: 16612637]
12. Spaide RF, Noble K, Morgan A, Freund KB. Vitelliform macular dystrophy. Ophthalmology 2006;113:1392–1400. [PubMed: 16877078]
13. Weingeist TA, Kobrin JL, Watzke RC. Histopathology of Best's macular dystrophy. Arch Ophthalmol 1982;100:1108–1114. [PubMed: 7092654]
14. Frangieh GT, Green WR, Fine SL. A histopathologic study of Best's macular dystrophy. Arch Ophthalmol 1982;100:1115–1121. [PubMed: 7092655]
15. Mullins RF, Oh KT, Heffron E, et al. Late development of vitelliform lesions and flecks in a patient with Best disease: clinicopathologic correlation. Arch Ophthalmol 2005;123:1588–1594. [PubMed: 16286623]
16. Bakall B, Radu RA, Stanton JB, et al. Enhanced accumulation of A2E in individuals homozygous or heterozygous for mutations in BEST1 (VMD2). Exp Eye Res 2007;85:34–43. [PubMed: 17477921]
17. Marmorstein AD, Marmorstein LY, Rayborn M, et al. Bestrophin, the product of the Best vitelliform macular dystrophy gene (VMD2), localizes to the basolateral plasma membrane of the retinal pigment epithelium. Proc Natl Acad Sci USA 2000;97:12758–12763. [PubMed: 11050159]
18. Marmorstein AD, Stanton JB, Yocom J, et al. A model of Best vitelliform macular dystrophy in rats. Invest Ophthalmol Vis Sci 2004;45:3733–3739. [PubMed: 15452084]
19. Rosenthal R, Bakall B, Kinnick T, et al. Expression of bestrophin-1, the product of the VMD2 gene, modulates voltage-dependent Ca^{2+} channels in retinal pigment epithelial cells. FASEB J 2006;20:178–180. [PubMed: 16282372]
20. Wachtmeister L, Dowling JE. The oscillatory potentials of the mudpuppy retina. Invest Ophthalmol Vis Sci 1978;17:1176–1188. [PubMed: 721390]
21. King-Smith PE, Loffing DH, Jones R. Rod and cone ERGs and their oscillatory potentials. Invest Ophthalmol Vis Sci 1986;27:270–273. [PubMed: 3943952]
22. Hood DC, Frishman LJ, Saszik S, Viswanathan S. Retinal origins of the primate multifocal ERG: implications for the human response. Invest Ophthalmol Vis Sci 2002;43:1673–1685. [PubMed: 11980890]
23. Holder GE. Significance of abnormal pattern electroretinography in anterior visual pathway dysfunction. Br J Ophthalmol 1987;71:166–171. [PubMed: 3828269]

Abbreviations

EOG	Electro-oculogram
Fd-OCT	Fourier-domain optical coherence tomography
ffERG	Full-field electroretinogram
ISCEV	

	International Society for Clinical Electrophysiology of Vision
mfERG	Multifocal electroretinogram
RPE	Retinal pigment epithelium

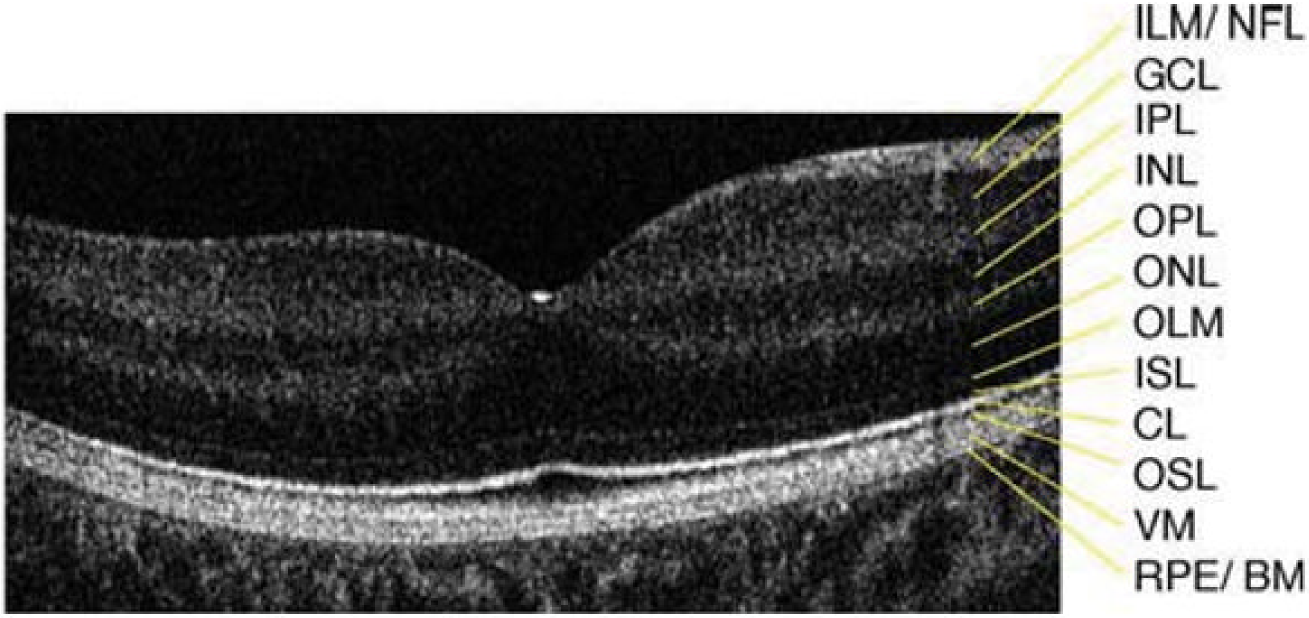

Fig. 1.

Six millimeter horizontal Fd-OCT scan through the right macula of a 9.3 year-old control subject. CL, connecting cilia; GCL, ganglion cell layer; ILM/NFL, internal limiting membrane/ nerve fiber layer; INL, inner nuclear layer; IPL, inner plexiform layer; ISL, inner segment layer; OLM, outer limiting membrane; ONL, outer nuclear layer; OPL, outer plexiform layer; OSL, outer segment layer; RPE/BM, retinal pigment epithelium/Bruch's membrane; VM, Verhoeff's membrane

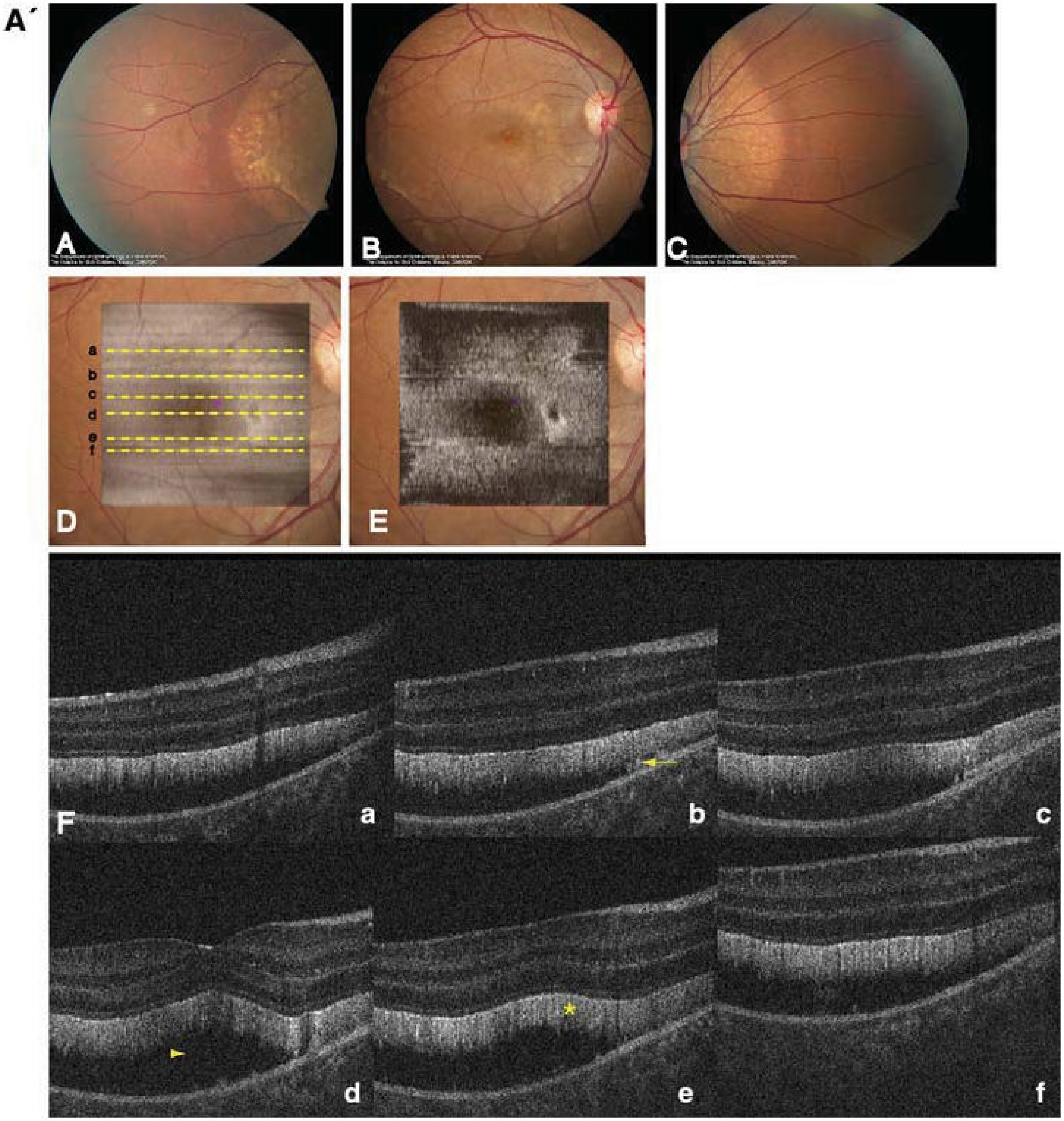
A´
A
B
C
a
b
c
d
e
f
D
E
F
a
b
c
d
e
f

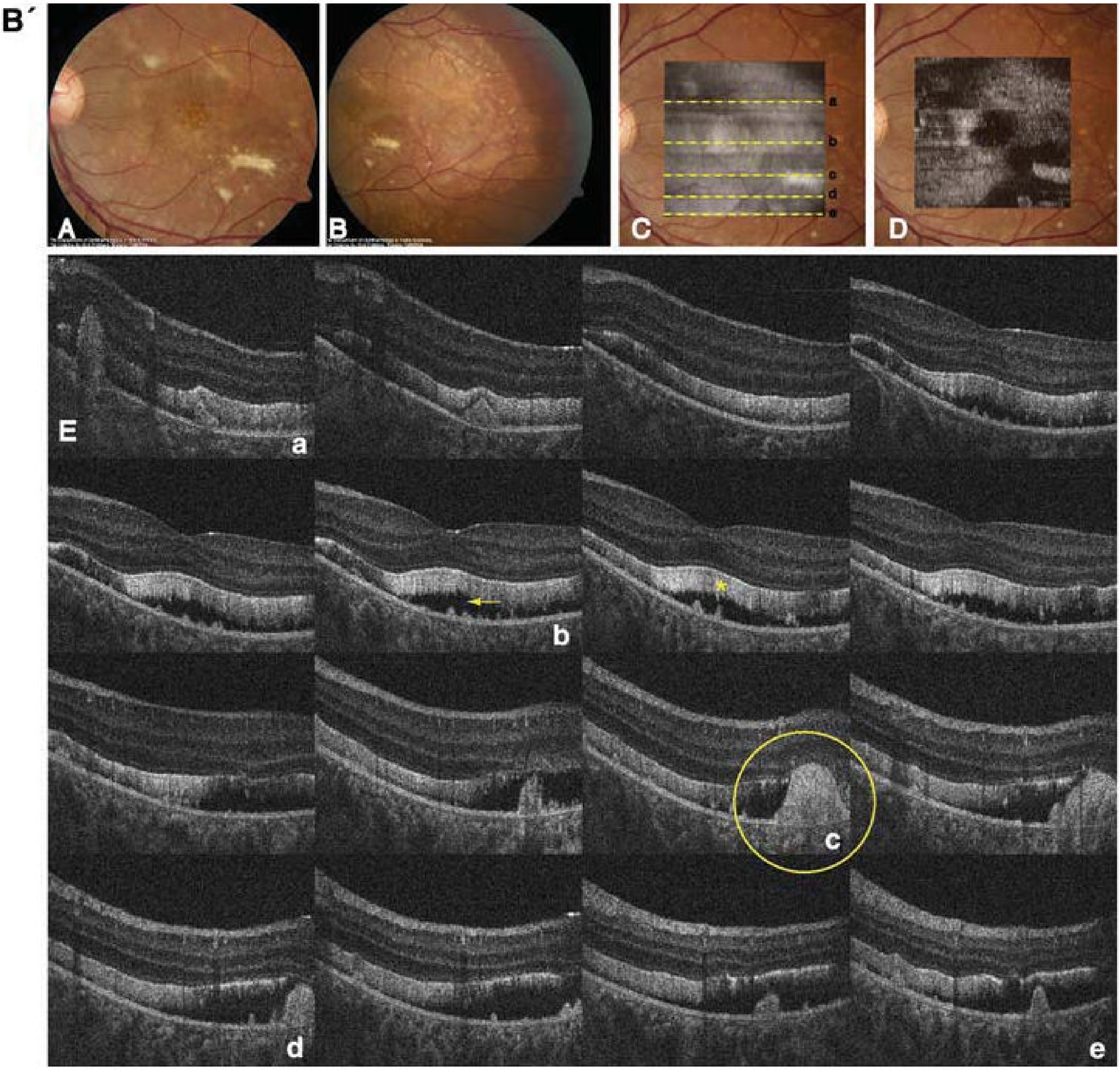

Fig. 2.

A' Composite of color fundus photographs and serial horizontal Fd-OCT scans (6 mm) of the right eye. Fundus photograph shows a well-demarcated area with round yellowish-white deposits at the posterior pole (A) extending to the temporal (B) and nasal (C) periphery. The locations of OCT B-scans are denoted by lines (*a*–*f*) shown on the OCT fundus image (intensity projection of the OCT volume), which is superposed and registered to the color fundus photo. (D) Virtual C-scan at the level of the photoreceptor inner/outer segment junction segmented from the reconstructed OCT volume is shown. (E) B-scans (F) illustrate deposits (denoted by an arrow in one scan) within the RPE with RPE detachment from the photoreceptors (arrowhead in one scan). Photoreceptor outer segments are thickened and elongated (indicated by a star in one scan). **B**' Composite of color fundus photograph and serial horizontal Fd-OCT scans (6 mm) of the left eye. Fundus photograph shows a well-demarcated area with round yellowish-white deposits at the posterior pole (A) extending to the temporal (B) and nasal (not shown) periphery. Subretinal fibrosis is visible inferior-temporal and superior-nasal of the fovea. The locations of OCT B-scans are denoted by lines (examples *a*–*e*) shown on the OCT fundus image, which is superposed and registered to the color fundus photo. (C) Virtual C-scan at the level of the photoreceptor inner/outer segment junction segmented from the reconstructed OCT volume is shown. (D) B-scans (E) demonstrate RPE detachment from the photoreceptors. Photoreceptor outer segments are thickened and elongated (indicated by a star in one scan). Small bridges between the photoreceptor outer segments and RPE are visible as denoted by an arrow in the scan through the fovea (b). Circle illustrates extensive RPE deposits extending to the outer plexiform layer

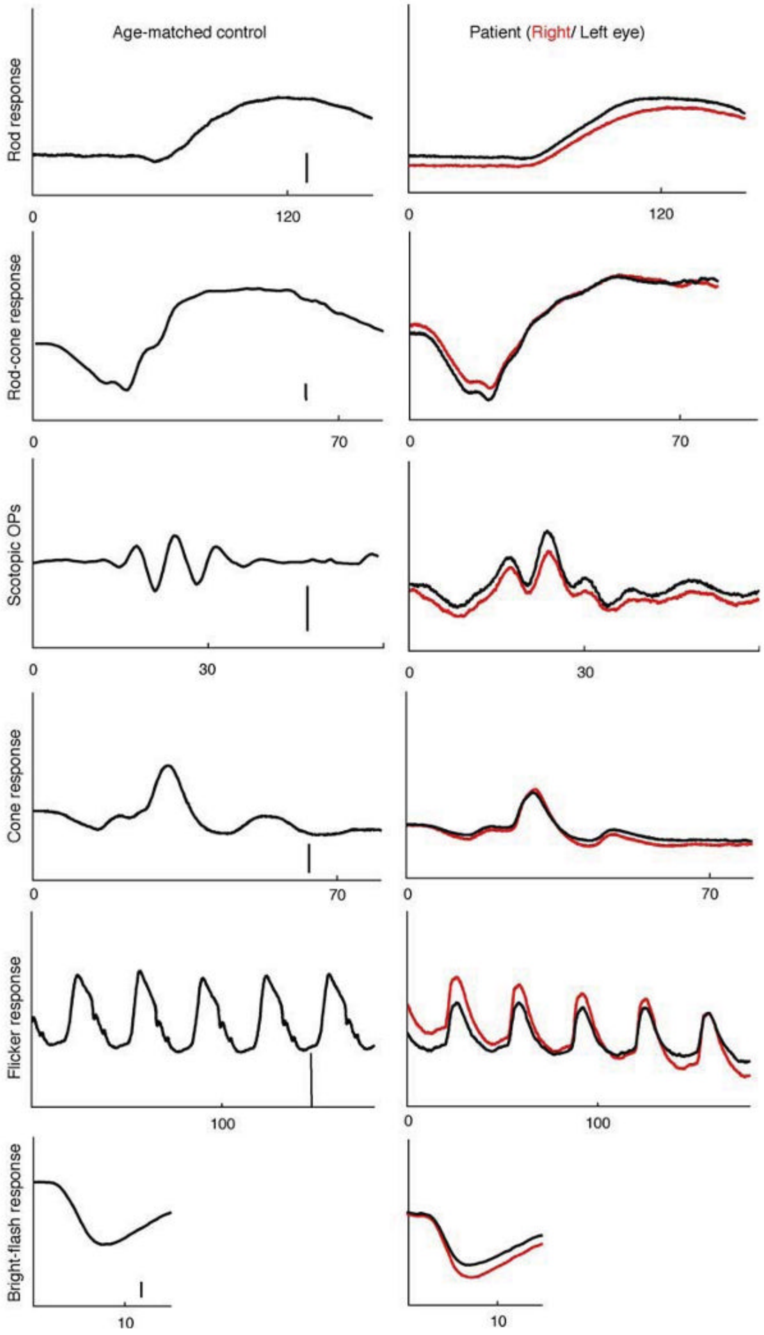

Fig. 3.

Full-field electroretinogram of the patient's right (red traces) and left eye (black traces) and an age-matched control (amplitude scale bar: 100 μV except OPs: 50 μV). The patient's rod and rod-cone b-wave responses are delayed in both eyes. (Table 1)

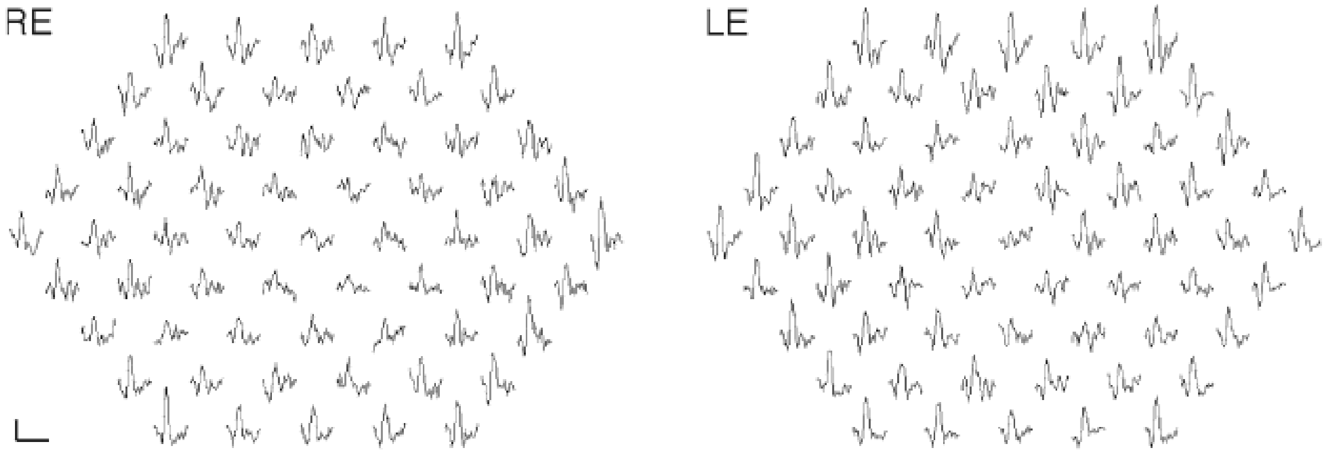

Fig. 4.

Multifocal electroretinogram traces from the right and left eye are shown. Responses within the central 10° are reduced (scale bar 200 nV, 80 ms)

Table 1

Vision function and electrophysiological data

	Normal value (age-matched)	**Right eye**	**Left eye**
Visual acuity (logMAR)	0.00	0.05	0.0
Contrast sensitivity (log)	1.65	1.5	1.5
Color vision (HRR test)		N	N
Visual field sensitivity			
Central		NA	Reduced
Peripheral		Normal	Normal
Full-field ERG responses	Normal range		
Rod b-wave			
Implicit time (ms)	101–129	132[a]	132[a]
Amplitude (μV)	106–384	273	284
Rod/cone a-wave			
Implicit time	17–23	21	21
Amplitude	150–398	332	302
Rod/cone b-wave			
Implicit time	38–52	56[a]	56[a]
Amplitude	381–760	595	560
Cone a-wave			
Implicit time	11–15	13	14
Amplitude	36–104	76	57
Cone b-wave			
Implicit time	30–35	33	32
Amplitude	111–292	195	156
Flicker			
Implicit time	23–29	28	28
Amplitude	53–176	119	91
OP sum			
Amplitude	43–249	236	125
Scotopic bright flash			
Implicit time	4.85–6.72	5.6	5.6
Amplitude	197–465	418	337
Multifocal ERG responses		Reduced and delayed within central 10°	
Electro-oculogram (Arden ratio)	≥2.0	1.0	1.3

HRR, Hardy–Rand–Rittler pseudoisochromatic plates; N, normal; NA, not analyzable

[a] Significantly delayed